ASME Open Journal of Engineering
Online journal at:
https://asmedigitalcollection.asme.org/openengineering

Swirl Brake Design for Improved Rotordynamic Vibration Stability Based on Computational Fluid Dynamics System Level Modeling

MD Shujan Ali[1]
Mem. ASME
Department of Mechanical Engineering,
Texas A&M University,
College Station, TX 77843
e-mail: md_shujan@tamu.edu

Farzam Mortazavi
Mem. ASME
Rotating Machinery Services Inc.,
Bethlehem, PA 18020
e-mail: farzam.mortazavi@tamu.edu

Alan Palazzolo
James J. Cain Professor I
Department of Mechanical Engineering,
Texas A&M University,
College Station, TX 77843
e-mail: a-palazzolo@tamu.edu

The accurate characterization of compressor rotordynamic coefficients during the design phase reduces the risk of subsynchronous vibration problems occurring in the field. Although rotordynamists extensively investigate discrete compressor components (such as seals and front shrouds) to tackle instability issues, integrated or system-level analysis of compressor rotordynamics is very sparse. In reality, the impeller, eye-labyrinth seal, and the front shroud heavily influence one another; and the collective dynamic behavior of the system differs from the sum of the dynamic behavior of isolated components. A computational fluid dynamics (CFD)-based approach is taken to evaluate the dynamic behavior of the system as a whole. The geometry and operating conditions in this work are based on the recent experimental study of Song et al. (2019, "Non-Axisymmetric Flows and Rotordynamic Forces in an Eccentric Shrouded Centrifugal Compressor—Part 1: Measurement," ASME J. Eng. Gas Turbines Power, 141(11), p. 111014. 10.1115/1.4044874) on centrifugal compressor. The commercial CFD code CFX 19.0 is used to resolve Reynolds-averaged Navier–Stokes equations to quantify the eye-labyrinth seal and front cavity stiffness, damping, and added mass. The entire compressor stage is modeled to uncover the coupled behavior of the components and assess the stability of the whole system instead of just discrete components. In the current work, three CFD approaches, namely quasi-steady, transient static eccentricity, and transient mesh deformation techniques are studied and benchmarked against analytical and experimental results from the literature. Having established the efficacy of the proposed approach, four types of swirl brakes are proposed and analyzed for stability. The novel swirl brakes create negative swirls at the brake cavities and stabilize both the front shroud and the eye-labyrinth seal simultaneously.
[DOI: 10.1115/1.4062934]

Keywords: compressor, eye-labyrinth seal, shroud, swirl brakes, rotordynamics, system-level, centrifugal compressors and pumps, computational fluid dynamics (CFD), flow-induced noise and vibration, fluid machinery, leakage, RANS simulations, transient analysis, turbomachines

1 Introduction

Labyrinth seals are widely used in high-performance centrifugal pumps and compressors as eye seals, end seals, and balance piston seals to reduce leakage loss and/or axial thrust [1,2]. Turbomachinery reliability, spin speed, and performance are often limited by their leakage flow path influence on rotordynamic stability. In an eccentrically operating rotor, non-axisymmetric flow inside the compressor eye-labyrinth seal, front cavity, and impeller blade passage give rise to rotordynamic forces. These fluid-induced forces may cause subsynchronous vibration which is undesirable and can even lead to catastrophic failure. Historically, the problem of subsynchronous vibration started to get broader attention after the incidence of such vibration instability at the space shuttle main engine high-pressure oxygen turbopump [3]. Rotordynamic performance of the leakage path has paramount importance as its normal force F_n can shift rotor critical speed while tangential force F_t may strongly affect pump/compressor stability.

Researchers and engineers have exerted tremendous efforts in the past 40 years to comprehend and enhance the rotordynamics of pump and compressor seals employing experiments [4–6] and predictive tools like bulk flow models [7,8] and computational fluid dynamics (CFD) [9,10]. In the rotordynamic analysis of shrouded compressors, most studies focus only on eye-labyrinth seal forces, and rotordynamics contribution of the front shroud is neglected. Similarly, pump stand-alone shroud forces [11,12] were measured using a shroud without blades and water as the working fluid. System-level analysis of compressors, treating seal and front cavity, as an integrated component and including all upstream

[1]Corresponding author.

Manuscript received April 5, 2023; final manuscript received July 5, 2023; published online July 25, 2023. Assoc. Editor: Jose Manoel Balthazar.

and downstream flow components in the analysis, is scant and limited.

System-level analysis of compressors is important for accurate assessment of their rotordynamic performance. The system-level analysis would be more relevant for future turbomachines featuring high spin speed and large energy density such as supercritical carbon dioxide (sCO_2) systems [13,14]. The sCO_2 compressor tested in Sandia National Laboratory operates at an astonishing spin speed of 75,000 rpm [13] and front shroud dynamic forces of such high-speed machines can be very high. The America Petroleum Institute (API) provides some guidelines to reduce vibrations in compressors and turbines by means of API 617 rotordynamic stability analysis [15]. API 617 Level 2 stability analysis is necessary when Level 1 stability analysis could not suppress the machine vibration. Level 2 stability analysis demands an assessment of destabilizing forces from all possible sources including impeller, seals, front shroud, and volute. System-level rotordynamic analysis is more suitable for API Level 2 stability analysis compared to any isolated seal analysis. The impeller, eye-labyrinth seal, and the front shroud heavily influence one another, and their collective behavior is different from the sum of their isolated components. The inlet/outlet boundary conditions for each component are interrelated and the components have coupled dynamic behavior. The API required stability analyses involve vibration studies using flexible, beam-based rotor models that include bearing stiffness and damping coefficients and lumped inertias for compressor and pump impellers [1]. Perhaps, most important are accurate values for stiffness, mass, and damping coefficients of seals and impellers. The aim of the present work is to present a general, CFD based, system-level modeling approach to enhance the predicted accuracy of these coefficients. In addition, novel swirl brake designs are proposed and shown to reduce destabilizing cross-coupled stiffness.

Flow swirl (circumferential component of velocity vector) at the seal inlet [12] significantly affects its rotordynamic forces. Swirl velocity at the seal inlet depends on upstream flow components, such as by geometry/curvature of the front cavity and volute [16]. Mortazavi and Palazzolo [16] numerically investigated the rotordynamic contribution of different volute shapes for a shrouded centrifugal pump and reported that the volute shape significantly alters rotordynamic forces of the whirling components such as seals, shrouds, and impellers. Uy and Brennen [11] experimentally tested three different shapes of isolated pump front shrouds rotating at 1000 rpm without any impeller blades and concluded that front shroud rotordynamic forces exhibit a strong correlation with fluid inlet swirl. Wagner et al. [17] experimentally measured the rotordynamic force of a compressor eye-labyrinth seal operating at 15,000 rpm with an inlet pressure of 1015 psi and compare their measurement with CFD predictions. In this study, the labyrinth seal was tested as an isolated component, and afterward, other upstream and downstream flow components, such as the inlet chamber, downstream annulus, end-plenum, and pre-swirl ring were added in the computational domain one by one. This study substantiated that not only the upstream cavity, but also downstream flow conditions affect overall seal force. Therefore, measurement or prediction of isolated eye-labyrinth seal forces is not adequate to design or troubleshoot a high-energy compression system. The system-level model captures the natural formation of flow swirl at the seal and shroud inlet, and it removes assumptions in vital boundary conditions. Furthermore, front cavity rotordynamic forces are not always negligible [18–20]. Gupta and Childs [21] employed a bulk flow model to study rotordynamic forces of a shrouded centrifugal compressor operating with methane at a running speed of 11,218 rpm, and reported that front cavity cross-coupled stiffness was trivial in this study compared to labyrinth seal contributions. Moore and Ransom [22,23] studied a four-stage centrifugal compressor working with nitrogen at a discharge pressure of 2300 psi and rotating at 21,500 rpm. Two of the four stages suffered subsynchronous vibration during tests. They utilized the quasi-steady CFD model to predict rotordynamic coefficients of the front shroud while they utilized the traditional bulk flow model in the seal region. Predicted shroud forces were comparable to that of the eye-labyrinth seal. Zhang et al. [19] predicted rotordynamic forces of the commercially available Solar's C51 shrouded centrifugal compressor using CFD by including the entire blade passage, eye-labyrinth seal, and front cavity into the computational domain. A quasi-steady CFD model of the whirling leakage path was employed, and the front cavity forces were observed to be greater than those of the eye seal in that analysis. Song et al. [20,24] measured direct and cross-coupled stiffness of a shrouded centrifugal compressor eye-labyrinth seal and front shroud cavity in the presence of the impeller blade passages, bell mouth suction, diffuser, and collector, unlike isolated seal tests. The compressor casing was moved to make the impeller statically eccentric. Counter to common conception, shroud cross-coupled stiffness was found to be 2.5 times larger than its seal counterpart. Hoopes et al. [18] utilize the transient CFD mesh deformation method to determine rotordynamic coefficients of the eye-labyrinth seal and front cavity of a shrouded centrifugal compressor. The impeller was modeled as a non-whirling component while the whirling motion was imposed on the eye seal and front cavity. The predicted cross-coupled stiffness for the front cavity was almost twice compared to that of the eye seal. Hence, there are disagreements on the relative importance of front cavity rotordynamic forces, and forces in the cavity can add uncertainty to the stability analysis if they are excluded. Furthermore, the shroud forces may become critical for future compressors operating at higher speeds, higher pressure ratios, and highly dense supercritical fluids. Higher spin speed forces the rotor to operate way above its first or even second critical speed and is prone to subsynchronous instabilities. At higher pressure ratios, pressure around the impeller increases which induces larger dynamic forces.

In recent times, due to the increase of available computational power, CFD has become a mainstream predictive tool in industry and academia to study impeller [9,10,25] and seal rotordynamics [16,26,27], automotive aerodynamics [28], and other flow devices [29,30]. Unlike bulk flow models [31], CFD models [32] do not rely on empirical correlations and can handle complex geometries that are impracticable for bulk flow models, rendering CFD an attractive candidate for detailed analysis of these components. Additionally, CFD can reveal complex flow details such as separation regions, local velocity, and pressure field. Literature on CFD models to conduct a system-level analysis of compressor rotordynamic forces is scarce in the open literature. This paper utilizes CFD to model the whole compressor stage in order to evaluate the coupled behavior of the components and assess rotordynamic coefficients of the whole system instead of just isolated components. The compressor geometry and experimental results from Ref. [20] have been utilized in the present work. This compressor has been selected because of available geometric details and operating conditions which are rare in the open literature. Non-axisymmetric pressure distributions and fluid swirl ratio inside the eye seal and front cavity, induced by the static eccentricity of the compressor impeller, are predicted along with dynamic forces. This study also aims to verify the accuracy of available CFD models, namely, quasi-steady, transient static eccentricity, and transient mesh deformation models, and used to predict rotordynamic forces in centrifugal pumps and compressors. Predictions of each CFD model are compared with experimental results and correlations from the literature. This paper also presents details of all three CFD methods utilized in this work. This work would serve as a guideline for system-level analysis of centrifugal pumps and compressors in general.

It is a well-established fact that the swirl (or circumferential velocity) of the secondary leakage path is one of the major causes of rotordynamic instabilities in centrifugal pumps [11,33,34] and compressors [35,36]. Swirl brakes [33,34,36,37], shunt injection [38], and hole-pattern seals [38,39] have been successfully implemented in the industry to reduce swirl at the seal inlet. Swirl brakes are a series of vanes installed circumferentially ahead of the seal entrance, or circumferentially cut grooves at the seal inlet, guiding the gas flow against rotor pre-rotation and dissipating

turbulent kinetic energy to reduce circumferential velocity. Circumferential slots (milled) are used as swirl brakes when there are clearance issues (such as rubbing) in putting additional metal strips at the seal inlet. Childs and Ramsey [37] utilized a vane-type swirl brake to stabilize an inter-stage seal in the high-pressure oxygen turbopump of the space shuttle main engine. It was a 20.2 cm diameter teeth-on-rotor labyrinth seal with a honeycomb seal operating with supply pressure up to 18.3 bar and rotating speed up to 16 krpm. Venkataraman et al. [36] designed a slot-type swirl brake for a commercially manufactured compressor equipped with a teeth-on-rotor labyrinth seal. It was a barrel-type compressor working with pressures varying from 2250 psia to 4500 psia at a maximum speed of 22,300 rpm. The swirl brake was formulated by milling several slots around the circumference of the seal ring. Three novel swirl brakes are presented here to demonstrate the improvements in design. Slots have been cut on the shroud stator instead of installing vanes to avoid rubbing. Their relative performance to reduce the leakage path swirl has been evaluated by employing the transient mesh deformation CFD model. These swirl brakes created negative swirls at the brake cavities, reduced whirl frequency ratio (WFR), and improved the stabilizing characteristics of both the front shroud and the eye-labyrinth seal simultaneously.

2 Rotordynamic Fluid Forces

The fluid-induced forces on a typical rotor are shown in Fig. 1. Figure 1(*a*) represents a statically eccentric rotor without any whirling motion. The rotor has been moved from the casing center by a small distance e. In Fig. 1(*b*), the rotor whirls about the casing center by a small eccentricity e. The shaft spins about its own center at angular velocity ω while it whirls about the casing center at angular velocity Ω. In both cases, rotordynamic forces can be decomposed into normal force F_n in the direction of the eccentricity, and tangential force F_t normal to the eccentricity. Normal force F_n typically has a centering effect and thus a negative normal force forms a positive direct stiffness K, that increases the pump/compressor critical speed. The circumferential force F_t impedes or propels rotor whirl, depending on the available direct damping and cross-coupled stiffness. A positive value of F_t may cause self-induced rotor instability as it feeds more energy to the forward whirling motion. In many applications, the inertia effect of F_n is small compared to the restoring forces of the bearing and the casing. Therefore, rotordynamic researchers often emphasize controlling the destabilizing tangential force.

Seal and front shroud stabilizing forces are often quantified using effective damping C_{eff} and effective stiffness K_{eff} defined as

$$\Omega C_{eff} = -\frac{F_t}{e} = -k + C\Omega + m\Omega^2 \tag{1}$$

$$K_{eff} = -\frac{F_n}{e} = K + c\Omega - M\Omega^2 \tag{2}$$

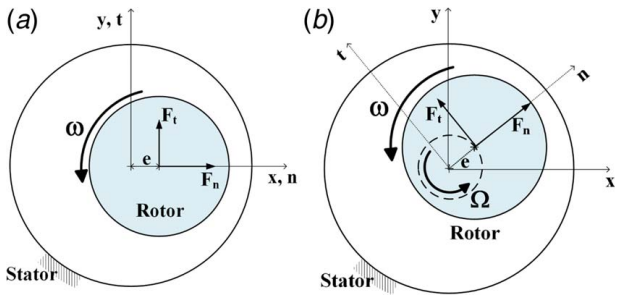

Fig. 1 Schematic of rotordynamic fluid forces: (*a*) statically eccentric rotor and (*b*) whirling rotor

Fluid forces are typically modeled in terms of stiffness, damping, and added mass coefficients. In the following sections of this study, this type of fluid force modeling will be referred to as the KCM model. These coefficients are readily used in rotordynamic analysis, such as in the determination of critical speed, unbalance response, stability analysis, etc. For this reason, these coefficients serve many purposes in industrial applications of turbomachinery to reduce vibration and maintain stable operations.

3 Geometry and Dimensions

The experimental works of Song et al. [20] and Song [24] are selected for verification purposes. Their geometry is utilized in this study as scholarly articles providing rotordynamic measurements along with considerable geometric and operating details are scarce in the open literature. A shrouded centrifugal compressor was tested with a static eccentricity of the impeller. The impeller was fixed while the casing was moved to induce non-axisymmetric flow in order to measure direct and cross-coupled stiffness values. Damping and virtual mass coefficients were not measured as no whirling motion was imposed on any of the components. Steady non-axisymmetric pressure distribution was measured using pressure taps placed at several axial and circumferential locations along the eye-labyrinth seal and the front cavity. The test rig contains a bell mouth suction ahead of the compressor wheel, and a long diffuser and circular collector following the impeller. The compressor impeller was redesigned using turbomachinery design software CFTURBO [40]. It provides the impeller design for desired geometric constraints and operating conditions. Unknown parameters such as blade angle and blade thickness distribution are estimated utilizing empirical functions, velocity triangle calculations, Euler equation solution, and blade blockage of the flow channel. Outflow slip coefficient is calculated based on the empirical formula of Aungier/Wiesner. The redesign process utilizes a free-form 3D blade shape coupled with conformal mapping to find impeller cross section and blade profile. The impeller geometry is inverse designed because the original geometry is the propriety data of the original equipment manufacturer (OEM) and is not available in the open literature. The redesign process introduced geometric uncertainties which are very difficult to quantify due to all geometric parameters. These uncertainties could be significant for estimating the aerodynamic properties, but these uncertainties have comparatively less influence on estimating the rotordynamic coefficients. Past research [10] has shown that a few key parameters, namely axial length of the rotor, fluid density, impeller outer radius, impeller discharge width, rotational speed, and eccentricity ratio, define the majority of rotordynamic forces. Mortazavi and Palazzolo [10] studied five different open impellers that have the same impeller outlet diameter, same tip clearance, same rotational speed, and number of blades, but they differ in their specific speeds. The operating conditions of each impeller set its specific speed which in turn determines blade angles, hub, and shroud profiles. They found that when normalizing the normal and tangential forces using the above-mentioned parameters, the force predictions of different impellers are almost on the same line, clearly showing that these are the key parameters.

The CFD computational domain keeps all the upstream and downstream flow components to model the coupled behavior of the system. The eye-labyrinth seal, front cavity, vaneless diffuser, and circular collector/volute are constructed using the dimensions provided in Ref. [20]. Table 1 lists design point data and geometric dimensions used to make the computational domain for this work. Figure 2 shows the computer-aided design (CAD) model of the test rig accommodating the impeller.

4 Numerical Methodology

4.1 Computational Domain. The exploded view of the computational grid is presented in Fig. 3. A full 360 deg model and

Table 1 Design point values and geometric dimensions

Parameters	Value
Rotational speed at design point, n_d	40,000 rpm
Number of blades, N	16
Mass flowrate, $\dot{m}$	0.5197 kg/s
Pressure ratio, Π	1.5
Inlet total pressure, p_{t0}	100.53 kPa
Inlet total temperature, T_{t0}	30 °C
Impeller exit diameter, D_4	153.24 mm
Rotor radius, R_r	46.79 mm
Impeller exit width, b_4	9.19 mm
Diffuser width at inlet, b_5	9.19 mm
Seal clearance, C_r	0.55 mm
Seal height, h	3.00 mm
Seal pitch, L_p	7.00 mm
Number of seal teeth, t	3
Tooth angle, α	156.10 deg
Shroud axial length, L_{shr}	23 mm
Shroud cavity height at inlet part, b_{shA}	1.38 mm
Shroud cavity height at exit part, b_{shC}	3.55 mm

mesh are required due to the non-uniform circumferential flow field and to resolve rotor forces resulting from static eccentricity or imposed whirling motion. The model incorporates the domains upstream and downstream to the seal and front cavity in order to capture the natural formation of flow swirl entering the seal and the front cavity. Furthermore, these subdomains enable correct modeling of pressure loss and recovery which affect the rotordynamic coefficients such as the direct stiffness. The presence of the blade passages transfers the blade passing effect to the front cavity.

Structured grids are used for all flow components except the collector. The collector is discretized utilizing an unstructured tetrahedral grid along with prism layers near the walls to resolve the boundary layer on the walls. The impeller grid is generated using ANSYS TURBOGRID. TURBOGRID provides the grid of a single-blade passage. That blade passage mesh was assembled and copied in the CFD solver to get the 360 deg impeller domain. Other structured grids are generated using ICEM CFD. Structured grids facilitate the reduction of overall mesh size without sacrificing numerical

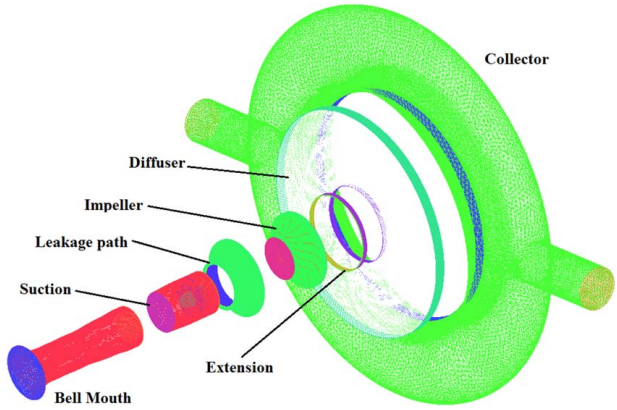

Fig. 3 Exploded view of the computational grid

accuracy, and help to avoid mesh inversion (negative mesh volume) in presence of mesh deformation boundary conditions. The computational grid has over 8.5 million nodes. The structured grid of the impeller and the leakage path is illustrated in Fig. 4.

4.2 Computational Fluid Dynamics Setup. The commercial code ANSYS CFX [41] is utilized to solve the 3D transient Reynolds-averaged Navier–Stokes (RANS) equations. Three rotordynamic modeling techniques, namely, quasi-steady, transient static eccentric, and transient mesh deformation models are utilized in this work. These models have some unique features that are discussed in the following sections. Table 2 contains other details of the CFD models. The working fluid is air ideal gas. The shear stress transport (SST) turbulence model has been selected as it is extensively benchmarked for turbomachines [42,43]. The forces were measured [20] for 36,000 rpm rotor spin although the impeller was designed for 40,000 rpm spin speed. All simulations are conducted with 36,000 rpm spin speed to be consistent with the experiment.

4.3 Dynamic Force Solution Technique. Rotordynamic coefficients are determined experimentally using static (see

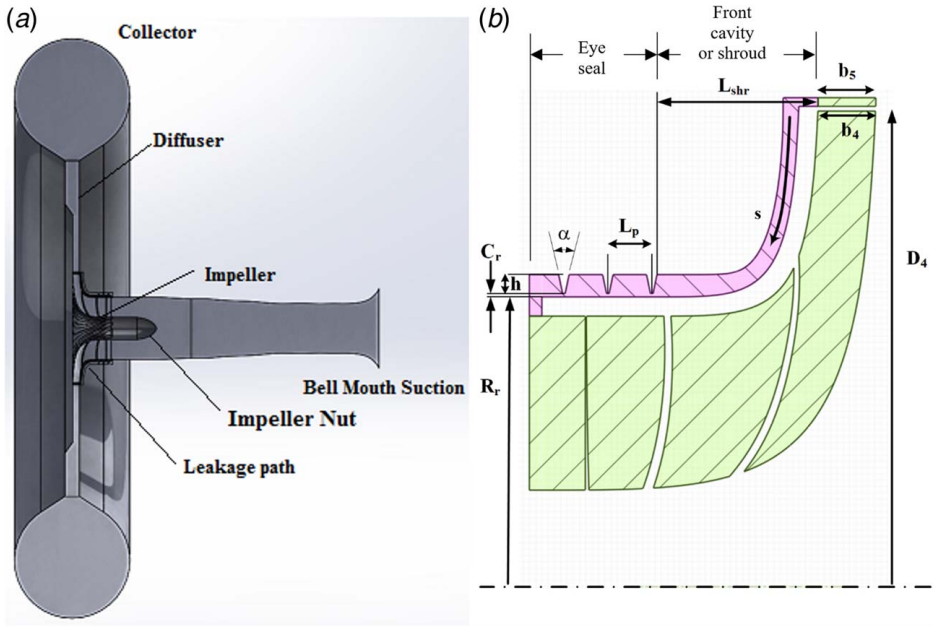

Fig. 2 CAD model of the compressor test rig: (*a*) cross section of the whole compressor stage and (*b*) cross section of the impeller, the eye-labyrinth seal, and the front shroud

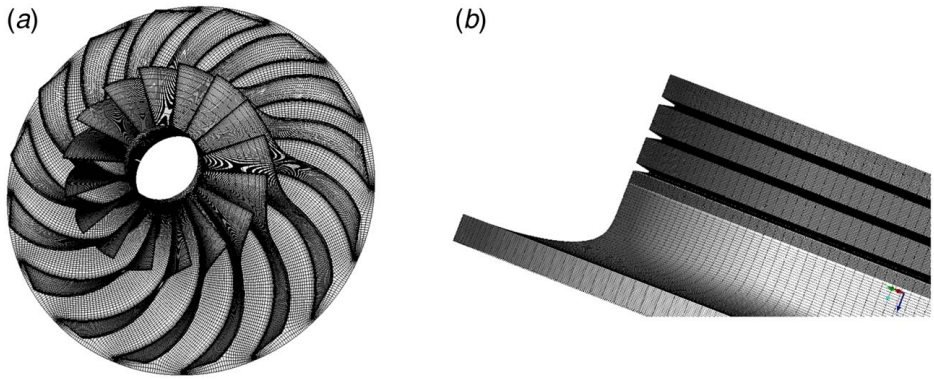

Fig. 4 Structured grid: (*a*) impeller and (*b*) the eye-labyrinth seal and front cavity

Fig. 1(*a*)) and dynamic tests (see Fig. 1(*b*)). Static tests provide direct and cross-coupled stiffness. A dynamic test provides not only stiffness but also damping and virtual mass coefficients. Similarly, there are several CFD models to numerically evaluate a pump/compressor with static eccentricity or dynamic whirling motion imposed on the rotor and/or the leakage path.

All CFD models, experimental measurements [20], and theoretical results [44] discussed in this work have utilized the assumption of frequency-independent rotordynamic coefficients and the skew-symmetric force model. Thus, only one set of direct and cross-coupled dynamic coefficients is required for stiffness, damping, and added mass terms. Applicability of the frequency-independent skew-symmetric force model for a shrouded centrifugal compressor [22,23], centrifugal pump [9–11], and eye-labyrinth gas seal [6,12,17–21,44] has been verified by prior theoretical [45,46], experimental, and CFD works.

4.3.1 Quasi-Steady Model. This model replicates dynamic testing using a circular whirl orbit. Like dynamic experiments, it provides stiffness damping and added mass coefficients. To quantify seal [19,47,48] and impeller rotordynamic forces [9], many authors have utilized this CFD model. This model is limited only to axisymmetric geometries and circular whirl orbits. This model cannot accommodate asymmetric components such as swirl brakes.

The transient whirling motion is converted to a steady problem by resolving the flow in a rotating frame centered at the casing center and rotating with the whirl speed Ω, as illustrated in Fig. 5. This frame would be referred to as the whirling frame for the remaining part of this paper. When observing from this reference frame, there is only the relative circumferential motion between the rotor and stator. In this rotating frame, the stator would rotate in opposite direction with the whirl speed $(-\Omega)$, and the rotor would spin at the speed of $(\omega - \Omega)$.

In this paper, the computational domain contains the primary flow path, which is spinning about its center (no static eccentricity or whirling), and upstream and downstream components. The primary path is resolved in the spinning frame of reference, the collector is resolved in the stationary frame, and all other subdomains are resolved in the whirling frame of reference. These domains are connected using sliding interfaces. Rotor eccentricity e is selected as $0.1C_r$ to comply with the small perturbation theory [1]. Forces generated by the eccentricity of the rotor are calculated by integrating pressure and shear stress around the rotor surface. In this problem, the eye seal and the front cavity are made eccentric in the y-axis for the quasi-steady model. The solution is obtained for nine whirl frequencies to get the map of impedance over various frequency ratios. When the normal and tangential forces are normalized by the whirl eccentricity e, this is called impedance and represents fluid reaction force per unit displacement/eccentricity. These impedances are compared with linear, second-order force models given by Eqs. (1) and (2). The radial and tangential impedances of the eye-labyrinth seal and the front cavity generated using the quasi-steady CFD model are presented in Fig. 6. These curves are similar to the previously presented impedance plots for centrifugal pumps [9] and compressors [22]. For both the labyrinth seal and the front cavity, the magnitude of effective stiffness and effective damping increases with increasing whirl frequency and follows a quadratic trend ($R^2 = 0.99$). The impedance curves contain significant curvature which indicates presence of added mass coefficients. The added mass coefficients are relatively small for the compressor since it operates with air.

4.3.2 Transient Static Eccentric Model. This CFD model predicts only direct and cross-coupled stiffness similar to the static eccentric experiments. The eye-labyrinth seal and the front cavity are made eccentric in the y-direction in the CAD model. The impeller is kept centered at the casing origin. So, the impeller has no eccentricity or whirling imposed.

First, a steady simulation has been done to be used as an initial condition for the transient analysis. Transient analysis has been done for at least 150 spin cycles and the first 30 spin cycles have been discarded for transient effects. The average force in the

Table 2 Computational fluid dynamics setup

Solution type	Transient
Working fluid	Air ideal gas
Rotational speed, n	36,000 rpm
Turbulence model	SST
	Automatic wall function
	High-speed wall heat transfer model
Heat transfer model	Total energy
Inlet boundary	Total pressure, static temperature
Outlet boundary	Mass flowrate
Advection scheme	High resolution
Transient scheme	Second-order backward Euler
Target residual	RMS, 10^{-5}
Wall properties	Adiabatic, smooth wall

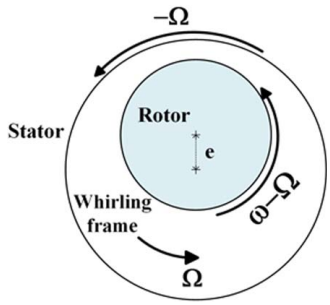

Fig. 5 Quasi-steady circular whirling motion in CFD

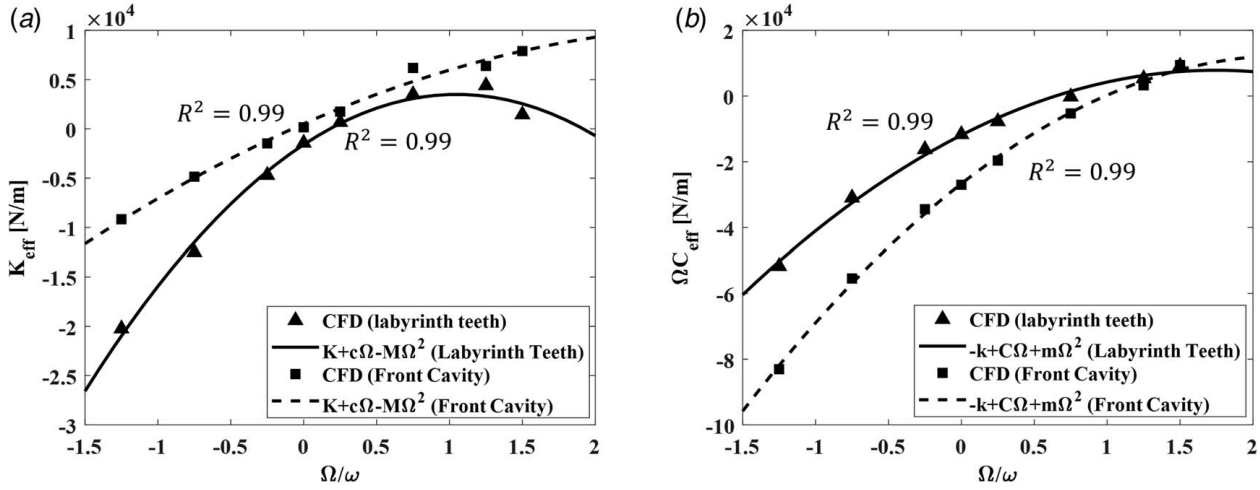

Fig. 6 Impedance and associated KCM model curve fit resulting from the quasi-steady CFD model: (*a*) effective damping and (*b*) effective stiffness

y-direction constitutes the normal force as the eccentricity is along the *y*-axis. The average force in the *x*-direction constitutes the tangential force. The direct and cross-coupled stiffness are defined as

$$K = \frac{\text{average}(F_y)}{e} \tag{3}$$

$$k = \frac{\text{average}(F_x)}{e} \tag{4}$$

4.3.3 Transient Mesh Deformation Model. This model predicts direct and cross-coupled stiffness, damping, and added mass coefficients, similar to dynamic experiments and the quasi-steady model. Furthermore, the transient modeling approach can accommodate any non-symmetric geometric features, such as asymmetric volute, diffuser vanes, swirl brakes, and shunt holes. In this method, in addition to spin speed, the whirling motion is imposed on the rotor surface as a transient periodic displacement utilizing the mesh deformation method [41]. A single-frequency circular whirl orbit has been utilized in this work. This use of transient mesh deformation based CFD models is well documented for predicting rotordynamic coefficients of seals [18,26] and impellers [10,25]. The imposed circular whirling motion about the centered position is described by

$$\Delta x = e\cos(\Omega t)\mathcal{H}\left(|\Omega|t - \frac{\pi}{2}\right) \tag{5}$$

$$\Delta y = e\sin(\Omega t) \tag{6}$$

where e denotes the eccentricity, Ω is whirl frequency, ω is spin speed, and $\mathcal{H}$ is a ramp function. The whirl frequency Ω is positive for a forward whirl and negative for a backward whirl. The ramp function $\mathcal{H}$ is introduced to the circular whirl motion to avoid rapid mesh distortion at the beginning of the simulations. Equations (5) and (6) are provided to the CFX CFD solver by means of a type of user-defined function called CEL (CFX Expression Language) [41]. The whirl radius e is kept under 10% of the seal clearance to be in the linear region of the motion. The transient forces on the eye-labyrinth seal and the front cavity are monitored during the transient solution of the model. The simulations are repeated for frequency ratios $\Omega/\omega = -1.5, -1.1, -0.5, 0.5, 1.1, 1.5$, in order to gather an adequate number of forces to perform the quadratic curve fit.

Due to the addition of mesh deformation boundary conditions, a diffusion equation is solved at each time-step [41]

$$\nabla \cdot (\Gamma_\delta \nabla \delta) = 0 \tag{7}$$

where the mesh displacement δ depends on the mesh stiffness parameter Γ_δ. Accurate mesh displacement boundary condition is important to avoid mesh inversion and failure of the simulation. Figure 7 shows mesh displacement boundary conditions for the eye-labyrinth seal and the front shroud. Whirling surfaces and stationary surfaces need to be connected using "parallel to boundary" conditions. This boundary condition allows the mesh elements to deform along the boundary surface but enforces them to remain in plane with their original location.

In the post-processing stage, the response of each frequency is extracted using the fast Fourier transform. Figures 8 and 9 show the plots of effective damping and effective stiffness as a function of the whirl frequency. CFD predicted data are curve fitted using the force model provided in Eqs. (1) and (2). The coefficients of the curve fits deliver constant stiffness, damping, and added mass coefficients. Both the effective damping and the effective stiffness increase with increasing whirl frequency in a quadratic trend. The effective stiffness curve of the shroud is linear with almost no curvature, indicating relatively small direct added mass coefficient. The effective damping C_{eff} indicates the magnitude and sign of the force that arise from cross-coupled stiffness. Negative values show that the evaluated component is destabilizing. The effective damping of the labyrinth seal and the front cavity becomes positive at about 2000 rad/s and 4000 rad/s, respectively. The frequency at which the effective damping curve change sign is called the cross-over frequency. At this frequency, the pressure field distribution changes such a way that the resultant force changes sign. The cross-over frequency is an industry-standard criterion for locating the first

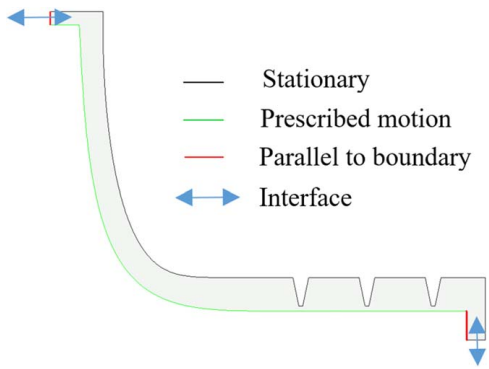

Fig. 7 Mesh displacement boundary conditions on the leakage path

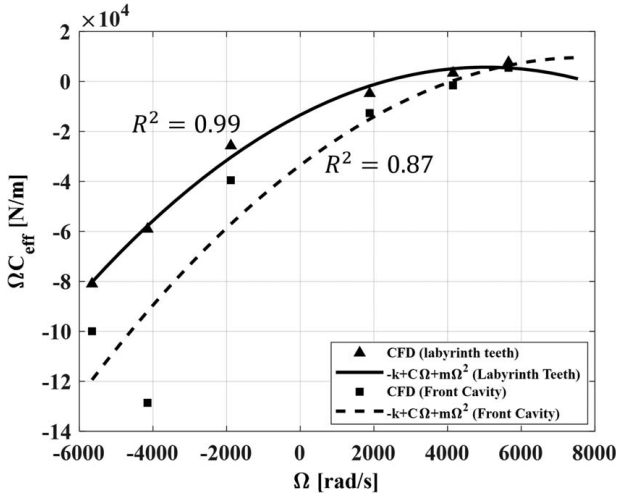

Fig. 8 Effective damping and associated KCM model curve fit resulting from the transient mesh deformation CFD model ($e = 0.1C_r$)

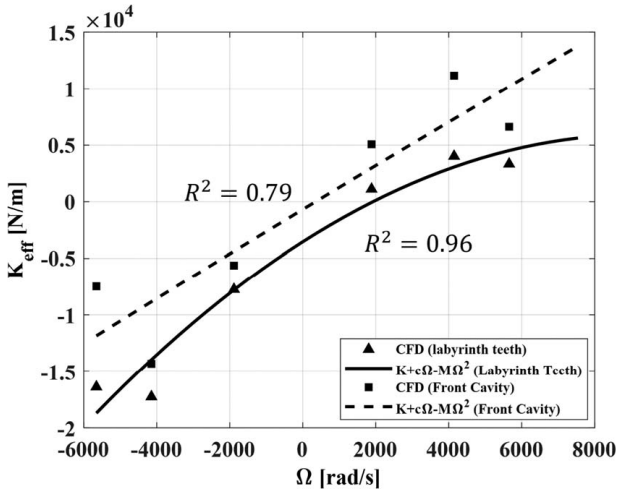

Fig. 9 Effective stiffness and associated KCM model curve fit resulting from the transient mesh deformation CFD model ($e = 0.1C_r$)

subsynchronous forward whirl rotor mode. If the rotor critical speed is below the crossover frequency, the machine would be at risk of subsynchronous rotor instability while operating supersynchronously above its critical speed and would be unable to operate at maximum speed.

4.4 Grid Independency Study. A grid analysis was conducted to ensure the independence of the results from spatial discretization. The consistency of the grid convergence error is calculated by three separate sets of parameters including: (1) compressor efficiency η, (2) pressure ratio Π, and (3) temperature ratio T_r. The first parameter depends on the resolution of boundary layers and wall shear stress, which usually require finer grids. The second parameter reveals the convergence of the pressure field and continuity equation. The third parameter reveals resolution of the energy equation. Figure 10 presents results of the grid independence study. The difference in results from these grids is less than 5%. The fine grid with 8.54 million nodes has been selected for all simulations. The resolution of the fine grid's subdomains is listed in Table 3. The leakage path mesh has over 2.6 million nodes and the impeller mesh has over 4.6 million nodes. Figure 11 illustrates the effect of grid size

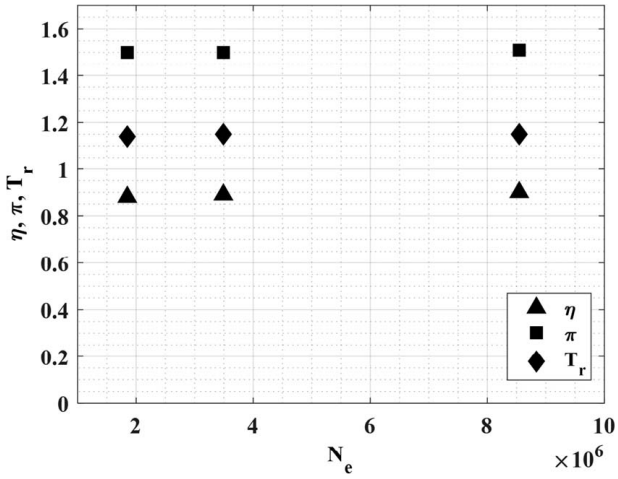

Fig. 10 Grid independence results

on dynamic forces for the transient mesh deformation CFD model. Rotordynamic forces for all grids almost lie on the same line. Hence, the fine grid would be sufficient for accurate resolution of rotordynamic forces. Furthermore, CFD-based calculations of rotordynamic forces show low sensitivity to mesh refinement since the primary contributor to the rotordynamic forces is the pressure [9,16,49] and fine resolution of shear stress is not so critical for such calculations [9].

5 Results and Discussion

5.1 Compressor Performance. The performance of the redesigned compressor impeller for concentric operation at the design point is shown in Table 4. The impeller pressure ratio is 1.5 which is the same as the design point. The pressure ratio is the ratio of total pressure at discharge to that at the inlet. Temperature ratio is defined as the ratio of total temperature at discharge to inlet total temperature. To visualize the flow field inside the concentric impeller, blade-to-blade views at three spanwise sections (span 0.1, 0.5, and 0.9) are shown in Fig. 12. The flow within each flow passage is identical as no eccentricity or whirling motion is applied in the primary passage and a symmetric ring-shaped collector is used. The homogeneous distribution of Mach number and pressure has a generally positive effect on efficiency and delay margin. However, this impeller has some relatively high Mach number regions in all three spanwise sections shown in Fig. 12(*c*). The maximum Mach number in these sections is about 0.66. The highest Mach number in all three sections was observed near the outflow region. The Mach number plot at 90% spanwise section also illustrates a recirculation zone. Unlike conventional volute, the ring-shaped collector induces no pressure asymmetry as shown in Fig. 13. Rotor forces are also close to zero (see Table 4) due to the symmetry of the pressure field.

Table 3 Subdomain grid size

Domain	N_e
Leakage path	2,623,608
Impeller	4,693,920
Suction	351,536
Bell mouth	156,800
Extension	35,100
Diffuser	331,580
Collector	352,780
Total	8,545,324

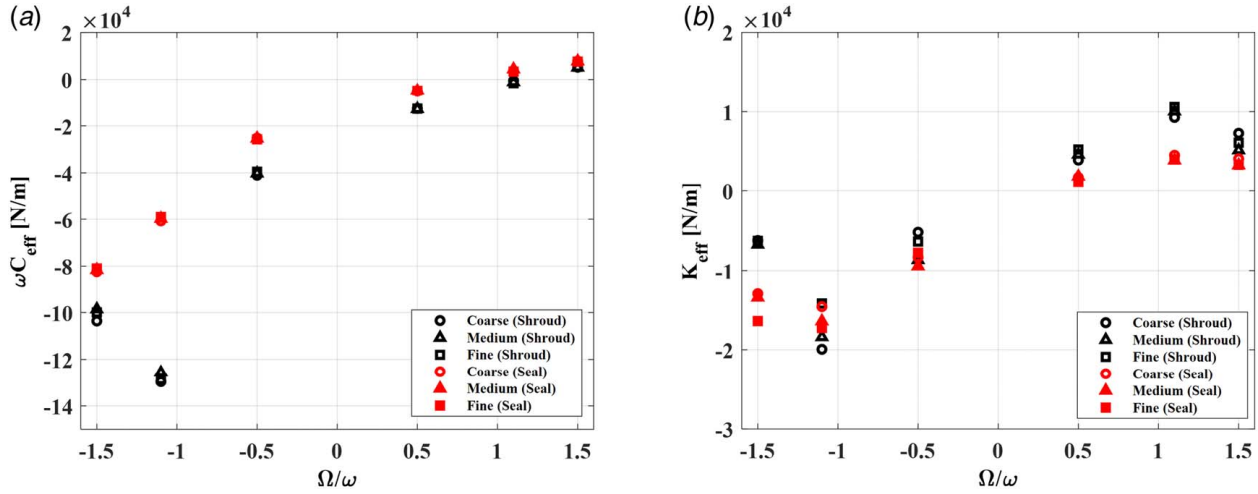

Fig. 11 Rotordynamic forces from various grid densities: (*a*) effective damping and (*b*) effective stiffness

Table 4 Performance of the redesigned impeller

Pressure ratio, Π	1.5
Efficiency, η	0.85
Temperature ratio, T_r	1.13
X-axis force, F_x	−0.06 N
Y-axis force, F_y	−0.03 N

5.2 Rotordynamic Forces. The prediction of rotordynamic coefficients using three different CFD models is listed in Table 5. In addition, Song et al. measured direct and cross-coupled stiffness values utilizing a static experiment [20] are also included, along with their predicted stiffness values using an analytical model [44]. CFD predictions are compared with these measurements and analytical model as well. Two of these CFD models, quasi-steady and transient mesh deformation models, also provide damping and added mass values. Predictions of damping are very close for both of these CFD models. Direct and cross-coupled damping are small compared to stiffness values, especially for subsynchronous frequencies. In all cases, the cross-coupled stiffness values are an order of magnitude larger compared to the direct stiffness. Direct stiffness, direct and cross-coupled damping in this compressor are negligible compared to typical bearing stiffness. In contrast, the cross-coupled stiffness coefficients may have a major effect on rotordynamic stability.

Prediction of stiffness values using transient mesh deformation model and transient static eccentric model is more accurate than the analytical model [44] and the quasi-steady CFD model. The transient mesh deformation model predicts cross-coupled stiffness values nearly equal to the experiment. Mortazavi and Palazzolo [16] also reported less accurate predictions from the quasi-steady CFD model compared to the transient whirling model for centrifugal pump application.

Rotordynamists in industry often time calculate shroud cross-coupled stiffness using correlations from Refs. [15,23,44,50,51]. CFD models used in this work are also compared with four such correlations in Table 6. Predictions from these correlations are far away from experimental measurements for the tested compressor. These correlations are designed based on few measurable parameters to do quick hand calculations, and as a result, they are not universal, accurate, or flexible for all kinds of machinery and operation regimes. Among tested correlations, only the API-Wachel formula [15] comes close to quasi-steady CFD model prediction.

Rotordynamic force (F) can be nondimensionalized as

$$\tilde{F} = \frac{F}{\rho_{ds} U_4^2 R_4^2} \tag{8}$$

Figure 14 shows a plot of nondimensional tangential force against eccentricity ratio ($\varepsilon = e/C_r$) for the static eccentric rotor. Forces reported in this figure are obtained using the transient static eccentricity CFD model (see Sec. 4.3.2) where the tangential force is calculated using Eq. (4). The tangential force has a linear relation with eccentricity for both the eye-labyrinth seal and the shroud. It validates the linearity assumption of rotordynamic forces and compliance of the CFD models with the small perturbation theory. Song et al. [20] obtained a similar linear relation in their experiment as shown in Fig. 14. CFD slightly underpredicts shroud tangential forces especially at larger eccentricity ratios. At high eccentricity ratios, the fluid reaction forces can exhibit some nonlinearity that cannot be properly predicted by CFD. Such large eccentricities do not occur in a physical machine, and it is a norm to keep the eccentricity small in CFD in order to follow the small perturbation theory [1,3,9,10]. Please note that the forces plotted in Fig. 14 were obtained using the transient static eccentricity method and even the predictions in Table 5 using this CFD model (column 5 of Table 5) show small deviations compared to experiment measurement of stiffness values. In Table 5, it was shown that the transient mesh deformation model (see Sec. 4.3.3) is better in predicting rotordynamic coefficients and shows an excellent agreement with the experimental measurements.

The damping predictions cannot be directly benchmarked due to a lack of experimental data. However, the authors have benchmarked the transient mesh deformation CFD method against experimental direct and cross-coupled damping coefficients for centrifugal pump open impeller [10,25], shrouded impeller [16], and teeth-on-rotor labyrinth seal [47]. In these references, both the stiffness and damping coefficients match well against experimental measurements.

The difference in results between the three CFD models stems from their underlying assumptions. The quasi-steady CFD model has some limitations in terms of transient and non-axisymmetric effects. Even earlier non-CFD theoretical models [45,46] have included transient effects that are not considered in the quasi-steady CFD model.

The transient static eccentricity method does not account for whirling motion and relies on forces on static eccentricity (zero whirling frequency) only. Results of this method come close to the transient mesh deformation CFD model and the experimental measurements for prediction of the cross-coupled stiffness.

The deviation in the prediction of the direct stiffness is largely due to the uncertainties in the front shroud curve. In addition, spatial and temporal numerical error, RANS turbulence modeling effects, unidentified surface roughness, numerical sampling duration/length, and curve fitting error contribute to model deviations.

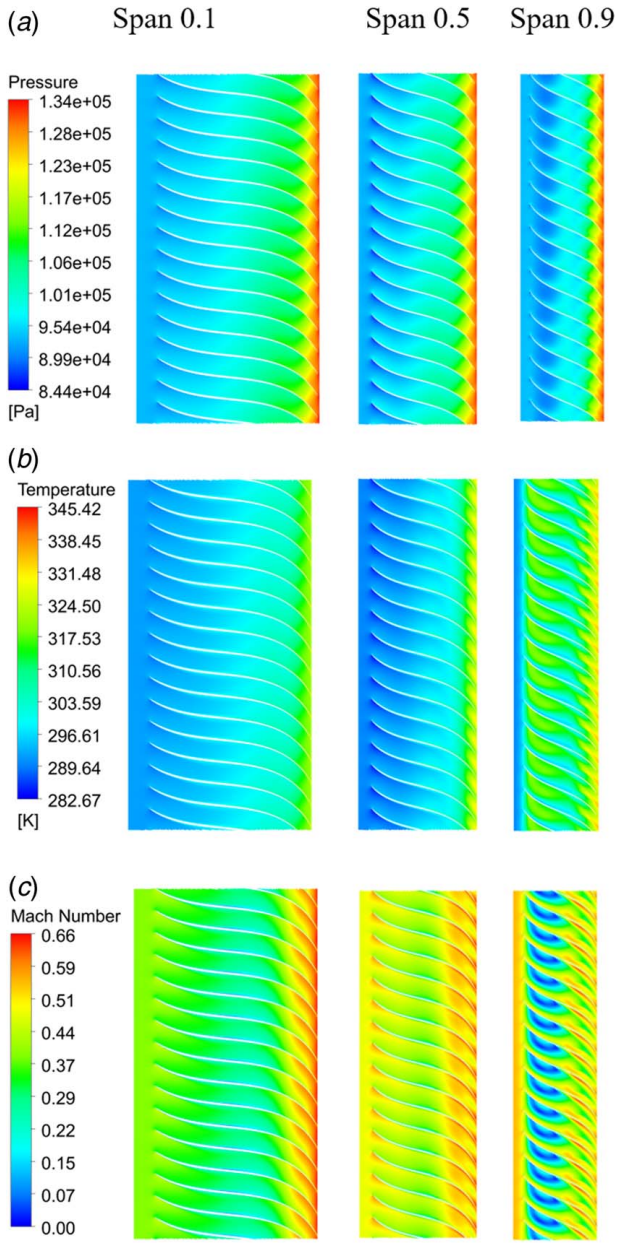

Fig. 12 Blade-to-blade view of the compressor primary flow path at $n = 36{,}000$ rpm: (*a*) pressure, (*b*) temperature, and (*c*) Mach number

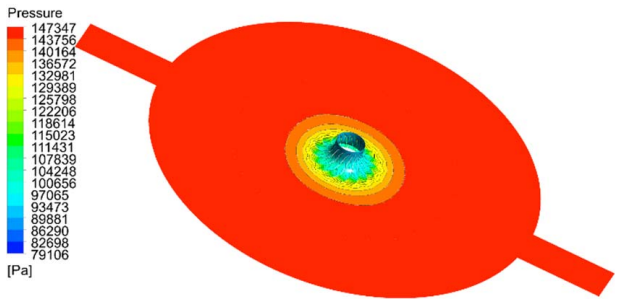

Fig. 13 Pressure contour at 50% span of the impeller and volute for concentric operation at $n = 36{,}000$ rpm

5.3 Axisymmetric Pressure. Pressure distribution ($P(s, \theta)$) at a particular meridional location can be decomposed into the axisymmetric mean ($P_m(s)$), and non-axisymmetric perturbation ($\delta P(s, \theta)$) as described in Eq. (9).

$$P(s, \theta) = P_m(s) + \delta P(s, \theta) \tag{9}$$

The mean pressure is the average of circumferential pressures at the particular meridional location, and it represents pressure due to a concentric rotor. The mean pressure is nondimensionalized by the blade exit pressure (P_4). Figure 15 presents nondimensional axisymmetric pressure versus nondimensional leakage meridional coordinate (s/S_{sh}) for frequency ratio $\Omega/\omega = 0.5$ obtained utilizing transient mesh deformation CFD model. S_{sh} is the length of the meridional shroud curve. Nondimensional leakage meridional coordinate $s/S_{sh} = 0$ represents the start of the shroud curve, and $s/S_{sh} = 1$ represents the start of the eye-labyrinth seal. $s/S_{sh} > 1$ represents meridional position in the eye-labyrinth seal region. The mean pressure drop in the shroud cavity is $\Delta P_{sh}/P_4 = 0.122$ which is higher than that in the eye-labyrinth seal $\Delta P_{seal}/P_4 = 0.108$. A similar trend was observed in the experiment [20] as well.

5.4 Non-Axisymmetric Pressure. The pressure difference between the concentric and eccentric/whirling rotor case is represented by the non-axisymmetric pressure perturbation. Non-axisymmetric pressure perturbations for the leakage path whirling at $e = 0.1C_r$ and frequency ratio $\Omega/\omega = 0.5$ are illustrated in Figs. 16 and 17. Figure 16 shows non-axisymmetric pressure perturbation as a function of the azimuthal angle at three meridional locations at the shroud—near the inlet ($s/S_{sh} = 0.22$), mid-part ($s/S_{sh} = 0.56$), and the shroud exit ($s/S_{sh} = 0.98$). Pressure perturbations inside the first and second cavities of the eye-labyrinth seal are shown in Fig. 17. Magnitude of the pressure perturbation is higher in the shroud cavity than that in the eye-labyrinth seal. This is expected as the mean pressure is much higher in the shroud cavity. Furthermore, there is no phase shift at various shroud path locations as illustrated in Fig. 16. However, phase shift is present along the seal (see Fig. 17). Similar trends were observed in previous experimental work [20,52].

5.5 Swirl Brakes. To enhance system-level stability, slots have been cut into the shroud stator (casing) to form swirl brakes. Four different configurations have been utilized. Figure 18 shows the designs of these swirl brakes and Table 7 provides their dimensions. The first brake is constituted by an axisymmetric slot as shown in Fig. 18(*a*). This design relies on sudden expansion of fluid before the eye-labyrinth seal inlet and this design is referred to as the "axisymmetric slot" for the remaining part of the paper. The second swirl brake design contains straight radial slots with an angle of $\gamma = 0$ deg as shown in Fig. 18(*b*). This design is referred to as "radial slots." The third set of swirl brakes are straight slots having a slot angle of $\gamma = 45$ deg as shown in Fig. 18(*c*). These slots are referred to as "angled slots." The fourth set of swirl brakes are aerodynamically shaped slots as shown in Fig. 18(*d*). These swirl brakes are referred to as "curved slots." All brake designs except the axisymmetric slot have utilized 23 slots. The design of curved slots is based on negating the average swirl component $\overline{v_\theta}$ at each meridional station along the impeller leakage path. The CFD solution of the baseline non-whirling case without any brakes (ideally axisymmetric flow inside the leakage path) is used to extract the swirl ($\overline{v_\theta}$) and meridional ($\overline{v_m}$) components of velocity. The velocity components are averaged along the normal direction to obtain the mean values. Once the mean values at the discrete meridional locations are known, a smooth profile has been fitted to the streamline to form the meanline of the swirl brake. The meanline can be exported to any CAD software to create the 3D shape by giving width and depth to the brake.

Geometry similar to the radial slots has been used before, primarily to reduce axial thrust [35,53]. The usage of radial slots, angled

Table 5 Comparison of prediction of rotordynamic coefficients

Parameter	Experiment [20]	Transient mesh deformation model (CFD)	Quasi-steady model (CFD)	Transient static eccentricity (CFD)	Analytical model [44]
Seal k (N/m)	1.34×10^4 (±790.6)	1.34×10^4	1.19×10^4	1.45×10^4	1.56×10^4
Shroud k (N/m)	3.35×10^4 (±1976.5)	3.35×10^4	2.67×10^4	3.87×10^4	3.14×10^4
Seal K (N/m)	-1.40×10^3 (±141.4)	-3.53×10^3	-1.60×10^3	2.49×10^3	3.91×10^3
Shroud K (N/m)	-3.54×10^3 (±254.9)	-1.12×10^3	5.18×10^2	-5.71×10^3	-7.06×10^3
Seal c (N · s/m)	—	2.05	2.58	—	—
Shroud c (N · s/m)	—	1.85	1.73	—	—
Seal C (N · s/m)	—	7.58	6.00	—	—
Shroud C (N · s/m)	—	11.13	9.18	—	—
Seal m (kg)	—	-7.50×10^{-4}	-4.56×10^{-4}	—	—
Shroud m (kg)	—	-7.20×10^{-4}	-5.39×10^{-4}	—	—
Seal M (kg)	—	1.11×10^{-4}	3.26×10^{-4}	—	—
Shroud M (kg)	—	-1.78×10^{-5}	7.46×10^{-5}	—	—

Table 6 Comparison of shroud cross-coupling prediction method

Method	k (N/m)
Experiment	3.35×10^4
Transient mesh deformation CFD	3.35×10^4
Transient static eccentricity CFD	3.87×10^4
Quasi-steady CFD	2.67×10^4
Analytical model [44]	3.14×10^4
Alford [51]	8.34×10^3
Wachel [50]	1.97×10^4
API-Wachel [15]	2.04×10^4
Moore et al. [23]	9.43×10^3

slots, and curved slots to improve the rotordynamic stability of the whole compressor stage is unique. Swirl brake slots act as reservoirs to trap fluid inside, create free vortices, and thus generate negative swirl. Since the majority of the inward leakage flows along the stator, the incoming flow to the seal has reduced swirl levels.

The swirl brakes are discretized using structured mesh generated in ICEM CFD. The quasi-steady model is not appropriate for study of radial slots and angled slots as it is limited to axisymmetric geometry. The transient static eccentricity model as well is less effective due to its inability to provide damping and added mass terms. The transient mesh deformation CFD model has been utilized to analyze the rotordynamic performance of the compressor stage in presence of the designed swirl brakes. The swirl ratio is used to quantify the effectiveness of the brakes in reducing swirl velocities inside the leakage path. The swirl ratio is defined as

$$\beta = \frac{v_\theta}{R\omega} \tag{10}$$

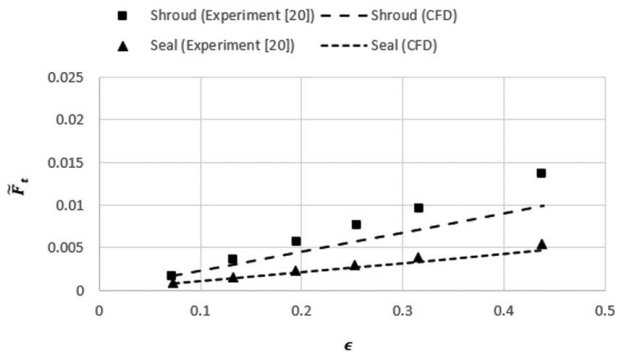

Fig. 14 Nondimensional tangential rotordynamic forces versus eccentricity ratio (transient static eccentricity CFD)

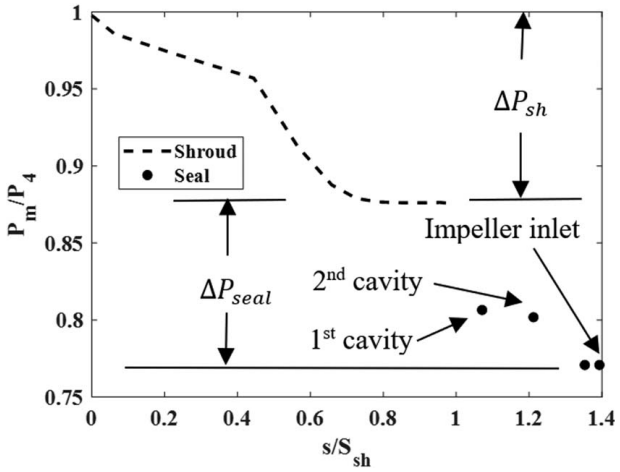

Fig. 15 Nondimensional axisymmetric pressure distribution versus nondimensional leakage meridional coordinate (transient mesh deformation CFD model)

Figure 19 provides the swirl ratio distributions inside the baseline design and proposed swirl brakes at particular axial locations. All swirl brake designs except the axisymmetric slot have induced negative swirl ratios inside the slot cavities. When the fluid's circumferential velocity is moving in the opposite direction to the rotor's spin

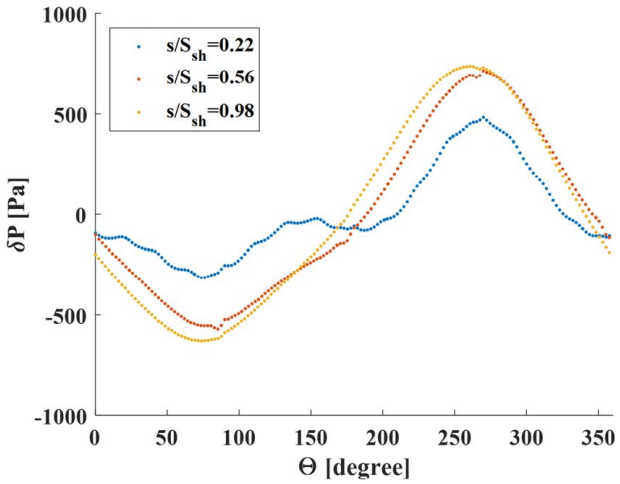

Fig. 16 Pressure perturbation in shroud cavity, $\Omega/\omega = 0.5$, $e = 0.1C_r$

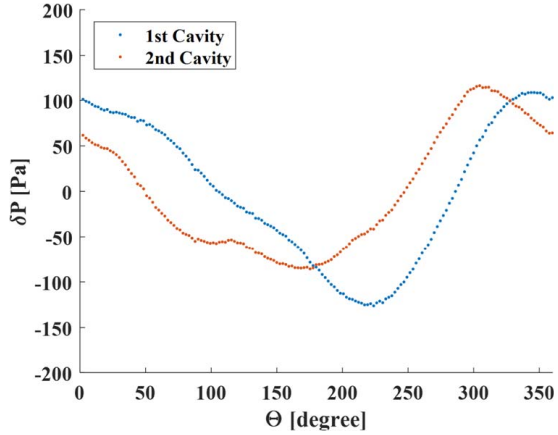

Fig. 17 Pressure perturbation in the eye-labyrinth seal, $\Omega/\omega = 0.5$, $e = 0.1C_r$

speed, the swirl ratio turns negative. The presence of negative swirl ratios reduces the average swirl ratio along the compressor leakage path. The negative swirl ratio is more pronounced inside the angled slots as shown in Fig. 19(*d*). At a particular meridional coordinate s, swirl ratio varies along the azimuthal angle. Maximum and average swirl ratios in the shroud and the eye-labyrinth seal have been plotted against the nondimensional meridional coordinate s/S_{sh} in Figs. 20 and 21. The average swirl ratio is determined by conducting circumferential averaging at a particular meridional location. The maximum swirl ratio represents the maximum value at a particular meridional location. Despite their simple design, radial slots have achieved the most significant results in reducing both the mean and maximum swirl ratio inside the shroud and the seal. At the shroud inlet, the mean swirl ratio is fixed at around 0.55 for all configurations of swirl brakes. The axisymmetric slot has an insignificant effect inside the eye-labyrinth seal but reduces both the mean and maximum swirl ratio inside the front shroud. All other brakes performed better than the axisymmetric slot in reducing both the mean and maximum swirl ratio inside the shroud and the seal.

The stability of a compressor stage is measured using the parameter called WFR f_ω [1]. It is defined as

$$f_\omega = \frac{k}{\omega C} \tag{11}$$

It is the ratio of destabilizing cross-coupled force to the stabilizing damping force present in the tangential force. The value marks

Table 7 Swirl brake dimensions

h_r (mm)	b_r (mm)	b_g (mm)	L_e (mm)	γ (deg)
10	15.87	2.5	2.67	0, 45

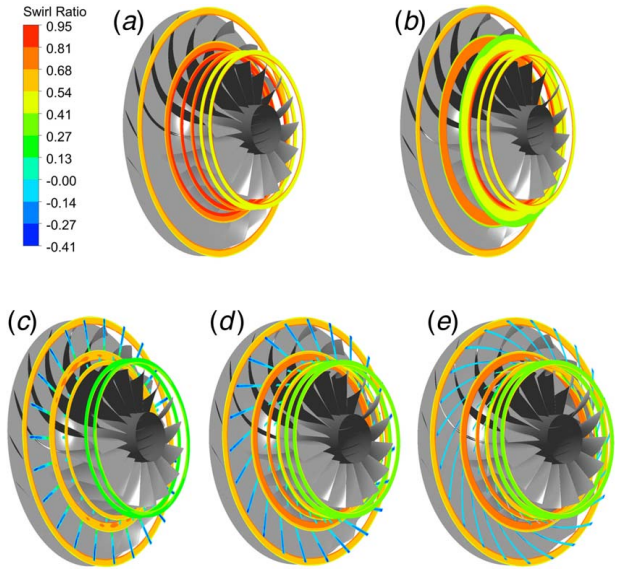

Fig. 19 Plot of swirl ratio for different swirl brake designs: (*a*) baseline design, (*b*) axisymmetric slot, (*c*) radial slots, (*d*) angled slots, and (*e*) curved slots

the frequency ratio that destabilizing and stabilizing tangential forces equate; therefore, a smaller f_ω value is favorable for stability. Since f_ω is correlated with the trapped fluid velocity inside the leakage path, a lower swirl ratio yields a lower WFR.

Table 8 lists the CFD predicted rotordynamic performance for the baseline design (no swirl brake) and the proposed swirl brakes. All proposed swirl brakes except the axisymmetric slot have reduced destabilizing cross-coupled stiffness k for both the shroud and the seal. Seal k and shroud k are minimums in the presence of radial slots as this configuration has reduced swirl ratio the most. Direct stiffness K has been increased for all swirl brake designs and shroud direct stiffness has become positive (stabilizing) for the angled slots and the curved slots. The presence of swirl brakes

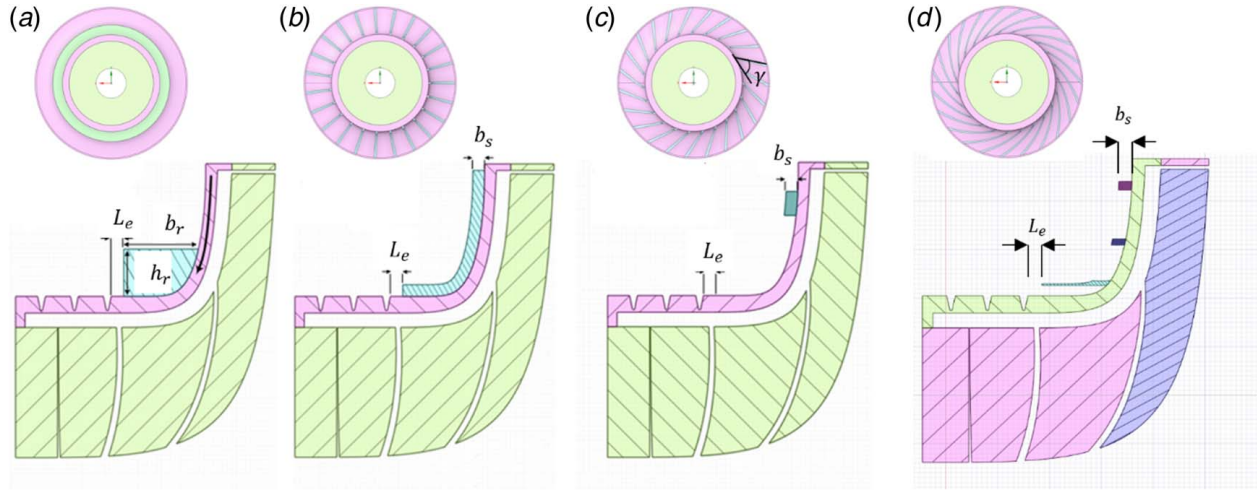

Fig. 18 Swirl brake designs: (*a*) axisymmetric slot, (*b*) radial slots, (*c*) angled slots, and (*d*) curved slots

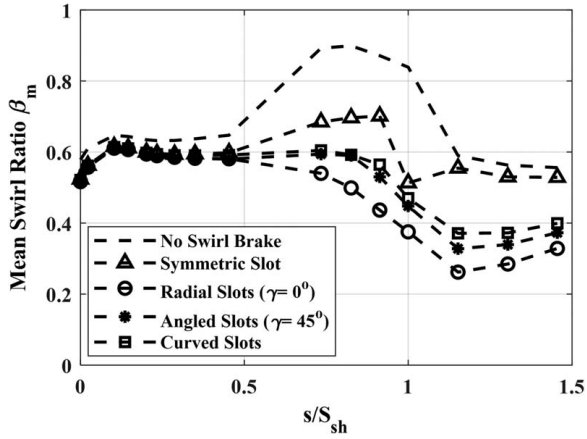

Fig. 20 Mean swirl ratio within the leakage path

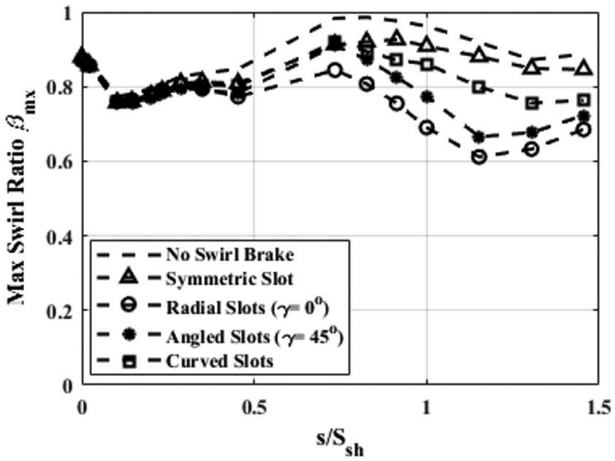

Fig. 21 Maximum swirl ratio within the leakage path

increases the effective clearance of the leakage path which results in smaller damping and mass coefficients. The reduction of swirl ratio along with the increase of effective clearance has caused a reduction of cross-coupled stiffness and an increase in direct stiffness. Furthermore, the brake slots reduce the average swirl inside the shroud cavity, diminishing dynamic pressure and raising static pressure. This effect partially increases seal direct stiffness by imposing a larger pressure differential across the seal and reinforcing the Lomakin effect. A well-designed swirl brake will stabilize the system by reducing the cross-coupled stiffness more than it will reduce the system's direct damping. Added mass and cross-coupled damping terms are not included in Table 8, as their values are small for all configurations tested.

All four of the designed swirl brakes have altered the WFR of both the front shroud and the eye-labyrinth seal. Isolated component-level models cannot resolve the flow physics and rotordynamic performance of such brakes. Hence, the system-level modeling approach is essential for the design and analysis of effective swirl control features.

The radial slots have lowered the whirl frequency ratio f_ω significantly for both the shroud and the eye-labyrinth seal. This is the best system-level swirl brake design among the designs studied for the rotordynamic stability of this particular compressor at the specified operating conditions. The performance of the angled slots and curved slots in stabilizing the system is also close to that of the radial slots as shown in Table 8. The axisymmetric slot has meaningfully improved WFR for the shroud, but the seal WFR has not benefited from this design compared to the baseline design.

Leakage reduction is one of the primary goals of labyrinth seals. The radial slots caused the seal to leak 16% more because they increased the pressure ratio of the seal. Hence, there is a trade-off between rotordynamic stability and seal leakage performance. In this study, the leakage rate for all proposed swirl brake designs is less than 3% of the compressor mass flow. The radial slots are the most stable while they also have the highest leakage rate among all designs. The slot height can be optimized to reduce the leakage to some extent. Disk friction loss and leakage poser loss were calculated for all swirl brake designs to assess their impact on compressor efficiency. Leakage loss is the work lost due to the leakage flow short-circuiting to impeller entrance not passing through the primary flow passage which has to be pressurized again. It is calculated using Eq. (12) where $\mathcal{P}_l$ is the leakage loss, H is fluid total enthalpy, $\dot{m}_l$ is the leakage mass flowrate, and $\dot{W}$ is the compressor total power. Disk friction loss arises from the fluid flowing through the rotating seal and shroud faces and the stationary casing. As the rotor rotates, friction is generated between the rotoring surface and the fluid medium surrounding it. Disk friction loss is the power required to overcome this friction. This is an important loss function for the design of high-speed turbomachines and is calculated according to Eq. (13). Here $\mathcal{P}_{df}$ is the disk friction loss, $\mathcal{T}_{disk}$ is the torque of the rotating surfaces, ω is the impeller rotating speed, and $\dot{W}$ is the compressor total power. As shown in Table 8, the leakage power loss and disk friction loss of all proposed swirl brake designs are very close to those of the baseline design. Any swirl brake designs proposed in this study exhibit less than 3% leakage loss and less than 1% disk friction loss. These swirl brakes do not have any drastic negative impact on the overall

Table 8 Rotordynamic performance of the designed swirl brakes (transient mesh deformation CFD model)

Parameter	Original geometry	Axisymmetric slot	Radial slots	Angled slots	Curved slots
No. of slots	0	1	23	23	23
Shroud k (N/m)	3.35×10^{4}	1.10×10^{4}	7.66×10^{3}	8.63×10^{3}	8.47×10^{3}
Seal k (N/m)	1.34×10^{4}	7.31×10^{3}	5.22×10^{3}	5.67×10^{3}	5.87×10^{3}
Shroud K (N/m)	-1.12×10^{3}	-1.42×10^{3}	-0.93×10^{3}	0.44×10^{3}	0.50×10^{3}
Seal K (N/m)	-3.53×10^{3}	-1.32×10^{3}	-0.99×10^{3}	-0.51×10^{3}	-0.46×10^{3}
Shroud C (N · s/m)	11.13	5.3	4.35	4.43	4.59
Seal C (N · s/m)	7.58	4.07	3.75	3.77	3.85
Shroud f_ω	0.8	0.55	0.47	0.52	0.49
Seal f_ω	0.47	0.48	0.37	0.40	0.40
Combined f_ω	0.66	0.52	0.42	0.46	0.45
$\dot{m}_l$ (kg/s)	1.34×10^{-2}	1.40×10^{-2}	1.54×10^{-2}	1.49×10^{-2}	1.44×10^{-2}
$\overline{v_{\theta,7}}$ (m/s)	168.42	100.98	67.63	80.68	84.61
$\mathcal{P}_l$ (%)	2.42	2.53	2.78	2.70	2.59
$\mathcal{P}_{df}$ (%)	0.80	0.81	0.95	0.90	0.84

performance of the compressor. These swirl brakes have no significant negative impact on the compressor's overall performance, particularly in terms of leakage losses and disk friction losses. The maximum Mach number within the seal and shroud was about 0.76 for any of the proposed swirl brake design and the baseline design.

$$\mathcal{P}_{\mathrm{l}} = \frac{\dot{m}_{\mathrm{l}}(H_4 - H_2)}{\dot{W}} \tag{12}$$

$$\mathcal{P}_{\mathrm{df}} = \frac{\mathcal{T}_{\mathrm{disk}}\omega}{\dot{W}} \tag{13}$$

6 Conclusion

The system-level analysis of centrifugal compressor rotordynamics incorporating all upstream and downstream flow components has been done by employing CFD. CFTURBO was employed to provide unavailable geometric features of the shrouded centrifugal compressor by Song et al. [20]. The performance of the redesigned impeller matches very well with the design point. Three different CFD models, namely, quasi-steady, transient static eccentricity, and transient mesh deformation models, were utilized to predict rotordynamic coefficients. The transient mesh deformation CFD model numerically imposes the whirling motion on the rotor and yields damping and added mass coefficients, along with stiffness coefficients. This CFD model performs better than the other CFD models and the analytical model [44] from the literature. The transient static eccentricity CFD model requires only a single transient simulation, and its stiffness prediction is superior to the quasi-steady CFD model and the analytical model. The quasi-steady CFD model results were not as accurate as those of the other CFD models, but its stiffness prediction was near the experimental measurements. Axisymmetric mean pressure and non-axisymmetric pressure perturbation inside the whirling eye-labyrinth seal and the front shroud were predicted with the transient mesh deformation CFD model. The rotordynamic forces have no phase shift inside the front shroud while they experience a phase shift inside the eye-labyrinth seal.

The test compressor cross-coupled stiffness magnitude is one order higher than direct stiffness, for both the eye-labyrinth seal and the front cavity. The cross-coupled stiffness of the front shroud cavity is higher than that of the eye-labyrinth seal. Thus, stability analysis requires a system-level analysis of the compressor rather than an isolated seal model. Compressor system-level analysis also facilitates accurate resolution of seal pre-swirl ratio and pressure field. System-level analysis minimizes uncertainty in compressor stability prediction even when the front cavity cross-coupled stiffness is insignificant.

Four novel swirl brakes are designed to reduce swirl velocities inside the leakage path. Radial slots cut at the shroud stator is the system-level swirl brake that improves the stabilizing characteristics of both the shroud and the seal. The radial slots have reduced the WFR of the front shroud and the eye-labyrinth seal by 41% and 21% respectively.

To develop a cohesive theory on the rotordynamics of shrouded centrifugal compressors, more studies are required. The test compressor has a small pressure ratio, and system-level analysis needs to be conducted on large pressure ratio and high-speed shrouded centrifugal compressors. The system-level analysis should be applied to sCO_2 compressors to understand the implication of high fluid density over shroud dynamic forces and determine the relative significance of shroud forces in these systems. The dynamic behavior of an impeller, seals, and front shroud becomes more important as the compressor head increases and pressure around the impeller and the rotor assembly increase. Isolated component models are inadequate to resolve system-level swirl brakes performance gain. The system-level modeling approach is essential for the design and analysis of sophisticated swirl control features.

Acknowledgment

The authors would like to thank CFTURBO[2] for providing the inverse design tools. Portions of this research were conducted with the advanced computing resources provided by Texas A&M High-Performance Research Computing.[3] This project was funded by the Turbomachinery Research Consortium (TRC)[4] at Texas A&M University. The authors would like to express their gratitude to TRC member companies for their continued support.

Conflict of Interest

There are no conflicts of interest. This article does not include research in which human participants were involved. Informed consent was not applicable. This article does not include any research in which animal participants were involved.

Data Availability Statement

The authors attest that all data for this study are included in the paper.

Nomenclature

- b = width (mm)
- c = cross-coupled damping coefficients (N · s/m)
- e = eccentricity (mm)
- h = seal tooth height (mm)
- k = cross-coupled stiffness (N/m)
- m = cross-coupled added mass (kg)
- n = rotor spin speed (rpm)
- s = leakage meridional coordinate (mm)
- t = number of seal teeth
- C = direct damping (N · s/m)
- D = diameter (mm)
- F = force (N)
- H = total enthalpy (J)
- K = direct stiffness (N/m)
- M = direct added mass (kg)
- N = number of impeller blades
- P = pressure (kPa)
- R = radius (mm)
- U = fluid velocity (m/s)
- $\dot{m}$ = mass flowrate (kg/s)
- $\tilde{F}$ = nondimensional force
- $\dot{W}$ = compressor power (W)
- b_{r} = axisymmetric slot (swirl brake) width (mm)
- b_{s} = height of the radial, angled, and curved slots (mm)
- f_{ω} = whirl frequency ratio
- h_{r} = axisymmetric slot (swirl brake) height (mm)
- p_{t0} = inlet total pressure (kPa)
- v_{θ} = circumferential velocity (m/s)
- C_{r} = seal radial clearance (mm)
- C_{eff} = effective damping (N · s/m)
- K_{eff} = effective stiffness (N/m)
- L_{e} = distance of swirl brake from seal inlet (mm)
- L_{p} = seal pitch (mm)
- L_{shr} = shroud axial length (mm)
- N_{e} = number of elements in the CFD grid
- S_{sh} = length of the meridional shroud curve (mm)
- T_{r} = temperature ratio
- T_{t0} = inlet total temperature (°C)
- $\mathcal{T}_{\mathrm{disk}}$ = leakage path (seal and shroud) torque (N · m)
- $\dot{m}_{\mathrm{l}}$ = leakage mass flowrate (kg/s)
- $\overline{v_{\mathrm{mr}}}$ = meridional velocity

[2] http://en.cfturbo.com/
[3] https://hprc.tamu.edu/
[4] http://turbolab.tamu.edu/trc/

$\overline{v_\theta}$ = average circumferential velocity (m/s)
$\mathcal{H}$ = step function
$\mathcal{P}_l$ = leakage power loss (%)
$\mathcal{P}_{df}$ = disk friction loss (%)
α = tooth angle (deg)
β = swirl ratio
δ = mesh displacement (mm)
δP = non-axisymmetric pressure perturbation (Pa)
ε = eccentricity ratio
η = efficiency
θ = azimuthal coordinate (deg)
Π = pressure ratio
ρ = density (kg/m^3)
ω = angular speed of rotor spin (rad/s)
Ω = angular speed of rotor whirl (rad/s)

Subscripts

0 = upstream
1 = impeller nut inlet
2 = impeller inlet, impeller nut exit
3 = blade inlet
4 = blade exit
5 = diffuser inlet
6 = shroud inlet
7 = seal inlet, shroud exit
8 = seal exit
d = design point
m = mean value
r = rotor
ds = discharge
mx = maximum value
sh = front shroud
n, t = normal and tangential directions in the whirling frame
x, y = x and y directions in the stationary frame

References

[1] Childs, D. W., 2013, *Turbomachinery Rotordynamics With Case Studies*, Minter Spring Publishing, Wellborn, TX.
[2] Brennen, C. E., 1994, *Hydrodynamics of Pumps*, Cambridge University Press, Oxford, UK.
[3] Childs, D. W., and Moyer, D. S., 1985, "Vibration Characteristics of the HPOTP (High-Pressure Oxygen Turbopump) of the SSME (Space Shuttle Main Engine)," ASME J. Eng. Gas Turbines Power, **107**(1), pp. 152–159.
[4] Marquette, O., Childs, D., and Philips, S., 1997, "Theory Versus Experiments for Leakage and Rotordynamic Coefficients of Circumferentially-Grooved Liquid Annular Seals With L/D of 0.45," ASME Paper No. FED SM97-3333.
[5] Iwatsubo, T., 1980, "Evaluation of Instability Forces of Labyrinth Seals in Turbines or Compressors," NASA Lewis Research Center Rotordynamic Instability Problem in High-Performance Turbomachinery, pp. 139–167 (SEE N80-29706 20-37).
[6] Childs, D. W., and Scharrer, J. K., 1986, "Experimental Rotordynamic Coefficient Results for Teeth-On-Rotor and Teeth-On-Stator Labyrinth Gas Seals," ASME J. Eng. Gas Turbines Power, **108**(4), pp. 599–604.
[7] Iwatsubo, T., and Sheng, B. C., 1990, "Evaluation of Dynamic Characteristics of Parallel Grooved Seals," Proceedings of the Third IFToMM International Conference on Rotor Dynamics, Lyon, France, Sept. 10–12, pp. 313–318.
[8] Marquette, O. R., and Childs, D., 1996, "An Extended Three-Control-Volume Theory for Circumferentially-Grooved Liquid Seals," ASME J. Tribol., **118**(2), pp. 276–285.
[9] Moore, J., and Palazzolo, A., 2001, "Rotordynamic Force Prediction of Whirling Centrifugal Impeller Shroud Passages Using Computational Fluid Dynamic Techniques," ASME J. Eng. Gas Turbines Power, **123**(4), pp. 910–918.
[10] Mortazavi, F., and Palazzolo, A., 2019, "A Transient Computational Fluid Dynamics, Phase Modulated, Multifrequency Approach for Impeller Rotordynamic Forces," ASME J. Fluids Eng., **141**(7), p. 071110.
[11] Uy, R. V., and Brennen, C. E., 1999, "Experimental Measurements of Rotordynamic Forces Caused by Front Shroud Pump Leakage," ASME J. Fluids Eng., **121**(3), pp. 633–637.
[12] Kirk, G., and Gao, R., 2012, "Influence of Preswirl on Rotordynamic Characteristics of Labyrinth Seals," Tribol. Trans., **55**(3), pp. 357–364.
[13] Wright, S., Conboy, T., and Rochau, G., 2011, "Break-Even Power Transients for Two Simple Recuperated S-CO_2 Brayton Cycle Test Configurations," Proceedings of SCO_2 Power Cycle Symposium, Boulder, CO, May 24–25.
[14] Cho, J., Shin, H., Ra, H. S., Lee, G., Roh, C., Lee, B., and Baik, Y. J., 2016, "Development of the Supercritical Carbon Dioxide Power Cycle Experimental in KIER," Proceedings of ASME Turbo Expo, Seoul, South Korea, June 13–17.
[15] API Standard, 2004, "Axial and Centrifugal Compressors and Expander-Compressors for Petroleum," Chemical and Gas Industry Services.
[16] Mortazavi, F., and Palazzolo, A., 2018, "Rotordynamic Force Coefficients of Volutes and Diffusers for Prediction of Turbomachinery Vibration," ASME J. Vib. Acoust., **140**(5), p. 051015.
[17] Wagner, N. G., Steff, K., Gausmann, R., and Schmidt, M., 2009, "Investigations on the Dynamic Coefficients of Impeller Eye Labyrinth Seals," Proceedings of the 38th Turbomachinery Symposium, Texas A&M University, Turbomachinery Laboratories.
[18] Hoopes, K., Moore, J. J., Rimpel, A., Kulhanek, C., and Venkataraman, B., 2019, "A Method for Rotordynamic Force Prediction of a Centrifugal Compressor Impeller Front Cavity Using a Transient Whirling CFD Technique," Proceedings of Turbo Expo: Power for Land, Sea, and Air, Phoenix, AZ, June 17–21.
[19] Zhang, D., Lee, C., and Cave, M., 2012, "A CFD Study on the Dynamic Coefficients of Labyrinth Seals," Proceedings of Turbo Expo: Power for Land, Sea, and Air, Copenhagen, Denmark, June 11–15, pp. 795–803.
[20] Song, J., Kim, S., Park, T. C., Cha, B.-J., Lim, D. H., Hong, J. S., Lee, T. W., and Song, S. J., 2019, "Non-Axisymmetric Flows and Rotordynamic Forces in an Eccentric Shrouded Centrifugal Compressor—Part 1: Measurement," ASME J. Eng. Gas Turbines Power, **141**(11), p. 111014.
[21] Gupta, M. K., and Childs, D. W., 2010, "Rotordynamic Stability Predictions for Centrifugal Compressors Using a Bulk-Flow Model to Predict Impeller Shroud Force and Moment Coefficients," ASME J. Eng. Gas Turbines Power, **132**(9), p. 091402.
[22] Moore, J. J., and Ransom, D. L., 2010, "Centrifugal Compressor Stability Prediction Using a New Physics Based Approach," ASME J. Eng. Gas Turbines Power, **132**(8), p. 082402.
[23] Moore, J. J., Ransom, D. L., and Viana, F., 2011, "Rotordynamic Force Prediction of Centrifugal Compressor Impellers Using Computational Fluid Dynamics," ASME J. Eng. Gas Turbines Power, **133**(4), p. 042504.
[24] Song, J., 2018, "Non-Axisymmetric Flow in a Shrouded Radial Compressor," Ph.D. thesis, Seoul National University, Seoul, South Korea.
[25] Ali, M. S., Mortazavi, F., and Palazzolo, A., 2020, "Flow Field Instability and Rotordynamic Impedances for an Open Impeller Centrifugal Pump in Transient Four-Quadrant Regimes," Proceedings of Turbo Expo: Power for Land, Sea, and Air, American Society of Mechanical Engineers, p. V10BT29A009.
[26] Li, Z., Li, J., and Yan, X., 2013, "Multiple Frequencies Elliptical Whirling Orbit Model and Transient RANS Solution Approach to Rotordynamic Coefficients of Annual Gas Seals Prediction," ASME J. Vib. Acoust., **135**(3), p. 031005.
[27] Ali, M. S., Mortazavi, F., and Palazzolo, A., 2021, "System Level Analysis of Compressor Eye-Labyrinth Seal Rotordynamic Forces: A Computational Fluid Dynamics Approach," Proceedings of the ASME Turbo Expo: Turbomachinery Technical Conference and Exposition, Virtual, Online, June 7–11.
[28] Faruqui, S. H. A., Ali, M. S., and Hossain, K. A., 2016, "Numerical Investigation of Aerodynamic Characteristics Over a Car for Optimizing the Shape of the Vehicle," Proceedings of the International Conference on Mechanical, Industrial and Energy Engineering, Khulna, Bangladesh, Dec. 26–27.
[29] Ali, M. S., Pandey, N., Hadj-Nacer, M., Greiner, M., and Riyad, M. F., 2021, "Parametric Study of Two-Phase Flow in a Porous Wick of a Mechanically Pumped Loop Heat Pipe," AIP Conf. Proc., **2324**(1), p. 050004.
[30] Ali, M. S., 2017, "Modeling of Heat Transfer and Flow Patterns in a Porous Wick of a Mechanically Pumped Loop Heat Pipe: Parametric Study Using ANSYS Fluent," Master's thesis, University of Nevada, Reno, NV.
[31] Hirs, G. G., 1970, *Fundamentals of a Bulk-Flow Theory for Turbulent Lubricant Films*, Delft University Holland, Netherlands.
[32] Versteeg, H. K., and Malalasekera, W., 2007, *An Introduction to Computational Fluid Dynamics: The Finite Volume Method*, Pearson Education, New York.
[33] Sivo, J., Acosta, A. J., Brennen, C., and Caughey, T., 1995, "The Influence of Swirl Brakes on the Rotordynamic Forces Generated by Discharge-to-Suction Leakage Flows in Centrifugal Pumps," ASME J. Fluids Eng., **117**(1), pp. 104–108.
[34] Benckert, H., and Wachter, J., 1980, "Flow Induced Spring Coefficients of Labyrinth Seals for Application in Rotor Dynamics," NASA Lewis Research Center Rotordynamic Instability Problem in High-Performance Turbomachinery.
[35] Baumann, U., 1999, "Rotordynamic Stability Tests on High-Pressure Radial Compressors," Proceedings of the 28th Turbomachinery Symposium, Texas A&M University. Turbomachinery Laboratories.
[36] Venkataraman, B., Moulton, D., Cave, M., Clarke, C., Moore, J., Wilkes, J., and Eldridge, T., 2018, "Design and Implementation of Swirl Brakes for Enhanced Rotordynamic Stability in an Off-Shore Centrifugal Compressor," Proceedings of Asia Turbomachinery & Pump Symposium, Turbomachinery Laboratory, Texas A&M Engineering Experiment Station.
[37] Childs, D. W., and Ramsey, C., 1991, "Seal-Rotordynamic-Coefficient Test Results for a Model SSME ATD-HPFTP Turbine Interstage Seal With and Without a Swirl Brake," ASME J. Tribol., **113**(1), pp. 198–203.
[38] Soto, E., and Childs, D., 1999, Experimental Rotordynamic Coefficient Results for (a) A Labyrinth Seal With and Without Shunt Injection and (b) A Honeycomb Seal".
[39] Moore, J. J., Walker, S. T., and Kuzdzal, M. J., 2002, "Rotordynamic Stability Measurement During Full-Load, Full-Pressure Testing of a 6000 psi Reinjection Centrifugal Compressor," Proceedings of the 31st Turbomachinery Symposium, Texas A&M University, Turbomachinery Laboratories.
[40] CFTurbo, 2021, *CFTurbo User Manual*, CFTurbo, Dresden, Germany.

[41] ANSYS, Inc., 2020, *ANSYS CFX-Solver Theory Guide, Release 2020R1*, ANSYS, Canonsburg, PA.
[42] Menter, F. R., Kuntz, M., and Langtry, R., 2003, "Ten Years of Industrial Experience With the SST Turbulence Model," Heat Mass Transfer, **4**(1), pp. 625–632.
[43] Menter, F. R., Smirnov, P. E., Liu, T., and Avancha, R., 2015, "A One-Equation Local Correlation-Based Transition Model," Flow Turbul. Combust., **95**(4), pp. 583–619.
[44] Song, J., and Song, S. J., 2019, "Non-Axisymmetric Flows and Rotordynamic Forces in an Eccentric Shrouded Centrifugal Compressor—Part 2: Analysis," ASME J. Eng. Gas Turbines Power, **141**(11), p. 111015.
[45] Tsujimoto, Y., Acosta, A., and Brennen, C., 1988, "Theoretical Study of Fluid Forces on a Centrifugal Impeller Rotating and Whirling in a Volute," ASME J. Vib. Acoust., **110**(3), pp. 263–269.
[46] Shoji, H., and Ohashi, H., 1987, "Lateral Fluid Forces on Whirling Centrifugal Impeller (1st Report: Theory)," ASME J. Fluids Eng., **109**(2), pp. 94–99.
[47] Mortazavi, F., and Palazzolo, A., 2018, "Prediction of Rotordynamic Performance of Smooth Stator-Grooved Rotor Liquid Annular Seals Utilizing Computational Fluid Dynamics," ASME J. Vib. Acoust., **140**(3), p. 031002.
[48] Moore, J. J., 2003, "Three-Dimensional CFD Rotordynamic Analysis of Gas Labyrinth Seals," ASME J. Vib. Acoust., **125**(4), pp. 427–433.
[49] Chochua, G., and Soulas, T. A., 2006, "Numerical Modeling of Rotordynamic Coefficients for Deliberately Roughened Stator Gas Annular Seals," ASME J. Tribol., **129**(2), pp. 424–429.
[50] Wachel, J., and Von Nimitz, W., 1981, "Ensuring the Reliability of Offshore Gas Compression Systems," J. Pet. Technol., **33**(11), pp. 2252–2260.
[51] Alford, J., 1965, "Protecting Turbomachinery From Self-Excited Rotor Whirl," J. Eng. Power, **87**(4), pp. 333–343.
[52] Benckert, H., 1980, "Strömungsbedingte Federkennwerte in Labyrinthdichtungen," Ph.D. thesis, University of Stuttgart, Stuttgart, Germany.
[53] Kurokawa, J., 2011, "J-Groove Technique for Suppressing Various Anomalous Flow Phenomena in Turbomachines," Int. J. Fluid Mach. Syst., **4**(1), pp. 1–13.